A Convective Heat-Transfer Model for Partial and Full Penetration Keyhole Mode Laser Welding of a Structural Steel

R. RAI, S.M. KELLY, R.P. MARTUKANITZ, and T. DEBROY

In the keyhole mode laser welding of many important engineering alloys such as structural steels, convective heat transport in the weld pool significantly affects temperature fields, cooling rates, and solidification characteristics of welds. Here we present a comprehensive model for understanding these important weld parameters by combining an efficient keyhole model with convective three-dimensional (3-D) heat-transfer calculations in the weld pool for both partial and full penetration laser welds. A modified turbulence model based on Prandtl's mixing length hypotheses is included to account for the enhanced heat and mass transfer due to turbulence in the weld pool by calculating spatially variable effective values of viscosity and thermal conductivity. The model has been applied to understand experimental results of both partial and full penetration welds of A131 structural steel for a wide range of welding speeds and input laser powers. The experimentally determined shapes of the partial and full penetration keyhole mode laser welds, the temperature profiles, and the solidification profiles are examined using computed results from the model. Convective heat transfer was the main mechanism of heat transfer in the weld pool and affected the weld pool geometry for A131 steel. Calculation of solidification parameters at the trailing edge of the weld pool showed nonplanar solidification with a tendency to become more dendritic with increase in laser power. Free surface calculation showed formation of a hump at the bottom surface of the full penetration weld. The weld microstructure becomes coarser as the heat input per unit length is increased, by either increasing laser power or decreasing welding velocity.

I. INTRODUCTION

DURING high power laser beam welding, a vapor cavity or a keyhole[1] often forms due to intense heating and vaporization of alloying elements. Keyhole mode laser welding is widely used in ship building, automobile industry, and many other manufacturing sectors for the welding of thick plates where low-distortion, clean autogenous welds with good surface finish are required. The dynamics of formation of the asymmetric keyhole, the intense vaporization of alloying elements from the keyhole, flow of molten metal in the weld pool, and two-phase mushy zone, melting, solidification, and heat transfer in the weldment, and the solid-state phase transformations make the physics of the welding process highly complex. In addition, the formation and movement of molten metal surfaces, such as the keyhole surface and the top surface of the weld pool, also affect the welding process. In the case of full penetration welds, an additional gas-metal surface also forms at the bottom of the workpiece.

Because of the complexity of the physical processes, earlier studies of keyhole mode laser welding considered mainly conduction heat transfer in the weld pool to understand the keyhole and the weld pool geometries.[2–9] These computationally efficient models ignored fluid flow, but found applications for the welding of high thermal conductivity alloys, such as aluminum alloys, where conduction is the main mechanism of heat transfer. However, these models cannot be applied to relatively low thermal conductivity alloys such as steel, because convection is usually the dominant mechanism of heat transfer. For these alloys, the fusion zone has a spread near the top surface due to convective heat transfer,[10] and is deep and narrow in the interior of the workpiece due to keyhole formation. Models that ignore convective heat transfer cannot predict this type of weld pool shape. On the other hand, comprehensive models that consider fluid flow and rigorously calculate the asymmetric keyhole geometry[11,12] require large computational time. A computationally efficient model capable of quantitatively examining the effects of convection on weld geometry, heat transfer, solidification, and microstructure that can be applied to both partial and full penetration welds remains to be developed.

Calculations of keyhole geometry considering fluid flow in gas, liquid, and the two-phase solid and liquid regions and tracking of the various gas/liquid free surfaces in the system involve significant computational effort. Therefore, some simplifications have been frequently made to make the computational task tractable. Dowden et al.[13–15] assumed a circular keyhole cross section of variable radius and modeled the liquid flow as

R. RAI, Graduate Student, and T. DEBROY, Professor of Materials Science and Engineering, are with the Department of Materials Science and Engineering and S.M. KELLY, Research Associate, and R.P. MARTUKANITZ, Senior Research Associate, Applied Research Laboratory, are with The Pennsylvania State University, University Park, PA 16802, USA.

horizontal flow around the keyhole and as axial motion between two coaxial cylinders. Klemens[16] considered the pressure-driven liquid metal flow resulting from vapor flow while ignoring the Marangoni convection. Sudnik et al.[17] simplified the fluid flow by approximating three-dimensional (3-D) fluid flow in the weld pool by two-dimensional flow in the horizontal and vertical sections. For partial penetration welds, Ki et al.[11,12] proposed a comprehensive model to predict the evolution of keyhole considering recoil pressure, multiple reflections, and fluid flow by tracking free surface movement at the gas/fluid interface.

Here we develop and test a computationally efficient heat-transfer and fluid-flow model of keyhole mode laser welding that can be applied to both partial and full penetration welds taking into account convective heat transfer in the weld pool. The keyhole profile is determined through point by point heat balance on the keyhole surface assuming boiling temperature at the surface. Energy and momentum transport equations are then solved in three dimensions in the entire weldment around the keyhole. A turbulence model, based on Prandtl's mixing length hypothesis, is used to predict the effective viscosity and effective thermal conductivity in the weld pool. The proposed model is computationally efficient because it can determine the asymmetric 3-D keyhole geometry by local heat balance on the keyhole wall. The deformed weld pool surface profile was iteratively determined by solving an appropriate energy balance equation. For full penetration welds, weld pool surface geometry was calculated at both the top and the bottom workpiece surfaces. The predicted weld geometries are compared with the corresponding experimentally determined results for the partial and full penetration welding of A131 grade EH-36 steel over a range of welding speeds and input laser powers. Steel was selected for model validation because it provides a system where convective heat transport is usually the main mechanism of heat transfer in the liquid weld pool. Calculations of free surface shape considering recoil pressure, gravitational force, and surface tension showed humps at the bottom surface of the full penetration welds. Solidification parameters at the trailing edge of the weld pool were calculated for varying welding speeds and input laser power to understand the effect of process parameters on solidification structure and microstructure.

II. EXPERIMENTS

Autogenous laser welds were made on A131 grade EH-36 steel (Table I) using a 14-kW maximum power continuous wave CO_2 laser (UTIL SM-21-14) at the Applied Research Laboratory, Penn State University. The raw laser beam, a 63.5-mm annulus, is focused onto the workpiece using a 330.2-mm focal length lens. The

Table II. Welding Variables for Experiments

Data set	Power (kW)	Welding Speed (mm/s)	Energy/Length (J/mm)
(a)	3.3	12.7	260
(b)	5.0	12.7	371
(c)	6.8	12.7	505
(d)	9.6	12.7	713
(e)	5.1	19.05	268
(f)	4.9	25.4	193
(g)	5.0	31.75	157

focal spot in the absence of plasma is approximately 1 mm in diameter. Laser power was measured at the workpiece prior to welding using a laser power probe. Power incident on the workpiece was varied from 3.3 to 9.6 kW and the welding speed varied from 12.7 to 31.8 mm/s. Table II lists the sets of laser-power and welding speed for which welds were prepared. The laser was focused on the surface of the plate and plasma suppression was provided by a helium shielding nozzle with a gas flow rate of 1.57×10^{-3} m^3/s. Samples were 10-mm thick, 51-mm wide, and 152 mm in length. The 127-mm long autogenous welds were centered on the plate. The top surface of the plate was ground to remove primer prior to welding. Selected welds were sectioned, polished, etched, and photographed to reveal the weld fusion zone profile and microstructure.

III. MATHEMATICAL MODEL

A. Calculation of Keyhole Profile

The keyhole geometry is calculated using a model that considers material properties, welding process parameters, and specimen geometry. Because the calculations of keyhole geometry and its application are available in the literature,[7,8] only the salient features of the model are presented in Appendix I. In short, the keyhole geometry was calculated based on local heat balance on the keyhole wall assuming multiple reflections of the laser beam within the keyhole. The number of reflections of the laser within the keyhole depended on the keyhole geometry, which was determined iteratively. The temperature at the keyhole wall was taken to be the boiling point of the alloy, which is defined as the temperature at which the equilibrium partial pressures of all elements add up to one atmosphere. Data used for the calculation of the keyhole geometry are listed in Table III.

The temperature distribution from the keyhole model was stored in a data file with all temperatures inside the keyhole assigned the boiling point temperature. This file was read in the thermo-fluid model and all points with a boiling point were considered within the keyhole. At each horizontal xy plane, the keyhole boundary is identified by a minimum and a maximum x value for any y value.

Table I. Specified Composition (Maximum Percent) of ASTM A131 Grade EH-and DH-36 Steels

C	Mn	Si	P	S	Al	Nb	V	Ti	Cu	Cr	Ni	Mo
0.18	1.6	0.5	0.035	0.035	0.015	0.05	0.10	0.02	0.35	0.2	0.4	0.08

Table III. Data Used in the Calculations

Physical Property	A131 Steel
Boiling point (K)	3100
Solidus temperature (K)	1745
Liquidus temperature (K)	1785
Density (kg/m³)	7200
Thermal conductivity (W/m K)	21
Beam radius at the end of the focusing lens (mm)	25
Beam radius at focal point (mm)	0.76
Focal length of lens (mm)	330
Heat of evaporation of Fe (J/kg)	6.52×10^6
Inverse Bremsstrahlung absorption coefficient (m^{-1})	100
Absorption coefficient (flat surface)	0.16
Molecular viscosity (Pa s)	0.0067
Coefficient of thermal expansion (1/K)	1.96×10^{-5}
Temperature coefficient of surface tension (N/m K)	-0.5×10^{-3}
Enthalpy of solid at melting point (J/kg)	1.20×10^6
Enthalpy of liquid at melting point (J/kg)	1.26×10^6
Specific heat of solid (J/kg K)	710.6
Specific heat of liquid (J/kg K)	836.0

B. Heat Transfer in the Weld Pool

After calculating the keyhole profile, the fluid flow and heat transfer in the weld pool is modeled by solving the equations of conservation of mass, momentum, and energy in three dimensions. The molten metal is assumed to be an incompressible, laminar, and Newtonian fluid. The liquid metal flow in the weld pool can be represented by the following momentum conservation equation:[18,19]

$$\rho \frac{\partial u_j}{\partial t} + \rho \frac{\partial (u_i u_j)}{\partial x_i} = \frac{\partial}{\partial x_i}\left(\mu \frac{\partial u_j}{\partial x_i}\right) + S_j \qquad [1]$$

where ρ is the density, t is the time, x_i is the distance along the ith (i = 1, 2, and 3) orthogonal direction, u_j is the velocity component along the j direction, μ is the effective viscosity, and S_j is the source term for the jth momentum equation and is given as

$$S_j = -\frac{\partial p}{\partial x_j} + \frac{\partial}{\partial x_j}\left(\mu \frac{\partial u_j}{\partial x_j}\right) - C\left(\frac{(1-f_L)^2}{f_L^3 + B}\right)u_j$$
$$+ \rho g \beta (T - T_{\text{ref}}) - \rho U \frac{\partial u_j}{\partial x_j} \qquad [2]$$

where p represents pressure, U is the welding velocity, and β is the coefficient of volume expansion. The third term represents the frictional dissipation in the mushy zone according to the Carman–Kozeny equation for flow through a porous media,[20,21] where f_L is the liquid fraction, B is very small computational constant introduced to avoid division by zero, and C is a constant accounting for the mushy zone morphology (a value of 1.6×10^4 was used in the present study).[23] The fourth term is the buoyancy source term.[22–24] The last term accounts for the relative motion between the laser source and the workpiece.[22]

The following continuity equation is solved in conjunction with the momentum equation to obtain the pressure field:

$$\frac{\partial (\rho u_i)}{\partial x_i} = 0 \qquad [3]$$

In order to trace the weld pool liquid/solid interface (*i.e.*, the phase change), the total enthalpy H is represented[25] by a sum of sensible heat h and latent heat content ΔH (*i.e.*, $H = h + \Delta H$). The sensible heat h is expressed as $h = \int C_p dT$, where C_p is the specific heat, and T is the temperature. The latent heat content ΔH is given as $\Delta H = f_L L$, where L is the latent heat of fusion. The liquid fraction f_L is assumed to vary linearly with temperature for simplicity:[22]

$$f_L = \begin{cases} 1 & T > T_L \\ \dfrac{T - T_S}{T_L - T_S} & T_S \leq T \leq T_L \\ 0 & T < T_S \end{cases} \qquad [4]$$

where T_L and T_S are the liquidus and solidus temperature, respectively. Thus, the thermal energy transportation in the weld workpiece can be expressed by the following modified energy equation:

$$\rho \frac{\partial h}{\partial t} + \rho \frac{\partial (u_i h)}{\partial x_i} = \frac{\partial}{\partial x_i}\left(\frac{k}{C_p}\frac{\partial h}{\partial x_i}\right) + S_h \qquad [5]$$

where k is the thermal conductivity. The source term S_h is due to the latent heat content and is given as

$$S_h = -\rho \frac{\partial (\Delta H)}{\partial t} - \rho \frac{\partial (u_i \Delta H)}{\partial x_i} - \rho U \frac{\partial h}{\partial x_i} - \rho U \frac{\partial \Delta H}{\partial x_i} \qquad [6]$$

The heat-transfer and fluid-flow equations were solved for the complete workpiece. For the region inside the keyhole, the coefficients and source terms in the equations were adjusted to obtain boiling point temperature and zero fluid velocities.

C. Boundary Conditions

A 3-D Cartesian coordinate system is used in the calculation, while only half of the workpiece is considered because the weld is symmetrical about the weld centerline. These boundary conditions are further discussed as follows.

1. Top surface
The weld top surface, except the keyhole region, is assumed to be flat. The velocity boundary condition is given as

$$\mu \frac{\partial u}{\partial z} = f_L \frac{d\gamma}{dT}\frac{\partial T}{\partial x}$$
$$\mu \frac{\partial v}{\partial z} = f_L \frac{d\gamma}{dT}\frac{\partial T}{\partial y}$$
$$w = 0 \qquad [7]$$

where u, v, and w are the velocity components along the x, y, and z directions, respectively, and $d\gamma/dT$ is the

temperature coefficient of surface tension. As shown in this equation, the u and v velocities are determined from the Marangoni effect.[26–29] The w velocity is equal to zero, because there is no outward flow at the pool top surface.

The heat flux at the top surface is given as

$$k\frac{\partial T}{\partial z}\bigg|_{\text{top}} = \frac{fQ\eta}{\pi r_b^2}\exp\left(-\frac{f(x^2+y^2)}{r_b^2}\right) \\ - \sigma\varepsilon\left(T^4 - T_a^4\right) - h_c(T - T_a) \quad [8]$$

where r_b is the beam radius, f is the power distribution factor, Q is the total laser power, η is the absorptivity, σ is the Stefan–Boltzmann constant, h_c is the heat-transfer coefficient, and T_a is the ambient temperature. In Eq. [8], the first term on the right-hand side is the heat input from the heat source, defined by a Gaussian heat distribution. The second and third terms represent the heat loss by radiation and convection, respectively.

2. Symmetric plane
The boundary conditions are defined as zero flux across the symmetric surface (*i.e.*, the vertical plane containing the welding direction) as

$$\frac{\partial u}{\partial y} = 0, \quad v = 0, \quad \frac{\partial w}{\partial y} = 0 \quad [9]$$

$$\frac{\partial h}{\partial y} = 0 \quad [10]$$

3. Keyhole surface
$$h = h_{\text{boil}} \quad [11]$$

where h_{boil} is the sensible heat of the steel at its boiling point. This represents that the keyhole surface is at the boiling temperature. The velocity component perpendicular to keyhole surface is assigned zero to represent no mass flux due to convection.

4. Bottom surface
For partial penetration welds, a convective heat-transfer boundary condition, with specified heat-transfer coefficient, is given. Because the weld pool does not extend to the bottom, the velocities are zero at the bottom surface. For full penetration welds, a flat bottom surface was assumed. Marangoni force-driven velocity boundary conditions were assumed at the bottom. The boundary conditions are given as

$$\mu\frac{\partial u}{\partial z} = f_L\frac{d\gamma}{dT}\frac{\partial T}{\partial x} \\ \mu\frac{\partial v}{\partial z} = f_L\frac{d\gamma}{dT}\frac{\partial T}{\partial y} \\ w = 0 \quad [12]$$

5. Solid surfaces
At all solid surfaces far away from the heat source, temperatures are set at ambient temperature (T_a) and the velocities are set to be zero.

D. Turbulence Model

During keyhole mode laser welding, the rates of transport of heat, mass, and momentum are often enhanced because of the presence of fluctuating velocities in the weld pool. The contribution of the fluctuating velocities is considered by an appropriate turbulence model that provides a systematic framework for calculating effective viscosity and thermal conductivity.[30,31] The values of these properties vary with the location in the weld pool and depend on the local characteristics of the fluid flow. In this work, a turbulence model based on Prandtl's mixing length hypothesis is used to estimate the turbulent viscosity:

$$\mu_t = \rho l_m v_t \quad [13]$$

where μ_i is the turbulent viscosity, l_m is the mixing length, and v_t is the turbulence velocity. The mixing length at any location within the weld pool is the distance traveled by an eddy before its decay and is often taken as the distance from the nearest wall.[31] In a controlled numerical study of recirculating flows in a small square cavity, the extent of computed turbulent kinetic energy was found to be about 10 pct of the mean kinetic energy.[32] Yang and DebRoy[33] computed mean velocity and turbulent energy fields during GMA welding of HSLA 100 steel using a two equation k-e model. Their results also show that the turbulent kinetic energy was of the order of 10 pct of the mean kinetic energy. The turbulent velocity v_t can therefore be expressed as

$$v_t = (0.1v^2)^{1/2} \quad [14]$$

$$\mu_t = 0.3\,\rho l_m v \quad [15]$$

Effective viscosity at a particular point is the sum of the turbulent (μ_t) and laminar (μ_l) viscosities (*i.e.*, $\mu = \mu_t + \mu_l$). The corresponding local turbulent thermal conductivities are calculated by using the turbulent Prandtl number, which is defined in the following relationship:

$$\text{Pr} = \frac{\mu_T c_p}{k_T} \quad [16]$$

For the calculations described here, the Prandtl number is set to a value of 0.9, based on previous modeling work.[27,31]

E. Free Surface Calculation

Free surface calculation was done based on constrained minimization of energy considering contributions from the gravitational energy, surface tension, and the recoil pressure of the metal vapors. The calculation of free surface neglects the effect of nonzero z direction fluid velocities.

The equations governing the top and the bottom free surface are given as[25,34,35]

$$P_{rec} + \lambda + \gamma \frac{\left(1+\phi_y^2\right)\phi_{xx} - 2\phi_x\phi_y\phi_{xy} + \left(1+\phi_x^2\right)\phi_{yy}}{\left(1+\phi_x^2+\phi_y^2\right)^{3/2}} = \rho g \phi$$

$$[17]$$

$$\lambda - \gamma \frac{\left(1+\psi_y^2\right)\psi_{xx} - 2\psi_x\psi_y\psi_{xy} + \left(1+\psi_x^2\right)\psi_{yy}}{\left(1+\psi_x^2+\psi_y^2\right)^{3/2}} = \rho g (\psi + L)$$

$$[18]$$

where P_{rec} is the recoil pressure, λ is the Lagrangian multiplier[36], γ is the surface tension, $\varphi_x = \frac{\partial \varphi}{\partial x}, \varphi_y = \frac{\partial \varphi}{\partial y}$, and $\varphi_{xy} = \frac{\partial \varphi}{\partial x \partial y}$. The symbols φ and ψ represent the depression of the top and bottom surfaces, respectively. The calculation of recoil pressure is described in Appendix II. The Lagrangian multiplier method[36] is used for the solution of a set of equations with constraints, such as volume conservation. Different values of the Lagrangian multiplier, λ, result in different surface configurations. The correct value of λ is determined from the volume conservation.

Volume conservation for partial penetration gives

$$\int\int \varphi\,dxdy = 0 \qquad [19]$$

For full penetration,

$$\int\int \varphi\,dxdy = \int\int \psi\,dxdy \qquad [20]$$

F. Calculation Methodology

(1) The keyhole geometry is calculated prior to starting the heat-transfer and fluid transport calculations. The procedure for the calculations is available in the literature.[7,8] The salient features of the model is described in brief in Appendix I.
(2) The computed keyhole geometry is mapped into the co-ordinate system of the thermo-fluid model (i.e., all grid points in the interior of the keyhole are identified).
(3) Momentum and energy balance equations, given by Eqs. [1], [3], and [5], are solved assuming boiling temperature at the keyhole surface and no mass flux across it.
(4) During calculations, the viscosity in the liquid phase is updated based on the turbulence model.
(5) The liquid pool boundary is identified by the solidus isotherm during calculation.
(6) Velocities and temperature inside the keyhole are fixed at zero and boiling point, respectively, by adjusting the source term coefficients using the control volume technique. The fluid velocities at the keyhole surface adjust accordingly so that there is zero mass flux across the keyhole walls.
(7) Free surface calculation is done using the temperature data from the thermo-fluid calculations.

G. Computational Time

The calculation domain was divided into nonuniform grids. The total number of scalar grid points used was approximately $170 \times 80 \times 60 = 816{,}000$. Computational time depends not only on the total number of grid points but also on the size of the weld pool. This is because the momentum conservation equations are solved only in the weld pool region. Thus, if the weld pool is large, the momentum conservation equations are solved at more grid points. The code was run on a desktop computer with 3.2 GHz, Pentium 4 processor, and 1 GB Ram, for 2000 to 3000 iterations to obtain convergence. For 9.6-kW input laser power and 12.7-mm/s welding speed, a full penetration weld of 10 mm was achieved and the total time taken for 3000 iterations was 29 minutes 4 seconds. On the other hand, for 5-kW input laser power and 31.8-mm/s welding speed, a partial penetration weld of 3.93-mm depth was achieved and the total time taken for 2000 iterations was 11 minutes 55 seconds. Thus, the calculation time was less than 30 minutes for all runs.

IV. RESULTS AND DISCUSSION

A. Weld Pool and Heat-Affected Zone Geometries

The weld pool simulation was carried out for laser powers between 3.0 to 10.0 kW and welding speeds between 12.7 and 31.8 mm/s. The comparison between the experimental and the simulated weld pool geometries is shown in Figures 1 and 2. The three lines in the figures indicate the solidus temperature (1745 K), the boiling point temperature (3100 K), and the A1 line temperature for the A131 alloy (1000 K). The boiling
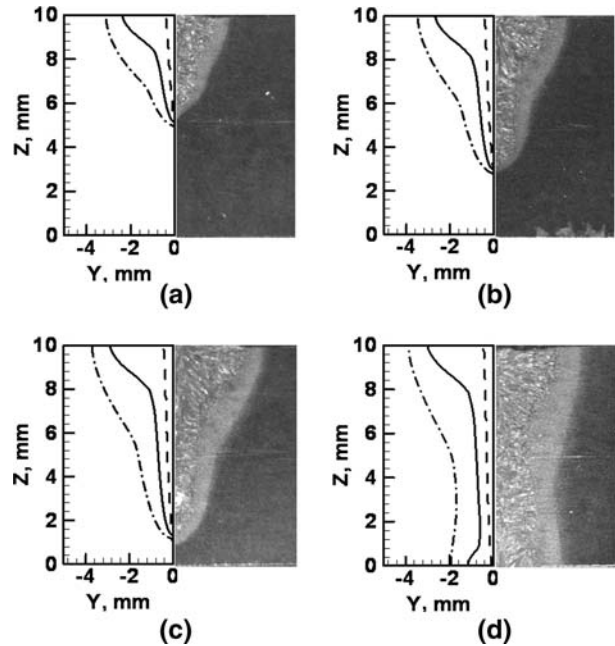

Fig. 1—Comparison of experimental and simulated weld cross sections for the A131 steel for a welding speed of 12.7 mm/s and powers of (a) 3.3 kW, (b) 5.0 kW, (c) 6.8 kW, and (d) 9.6 kW.
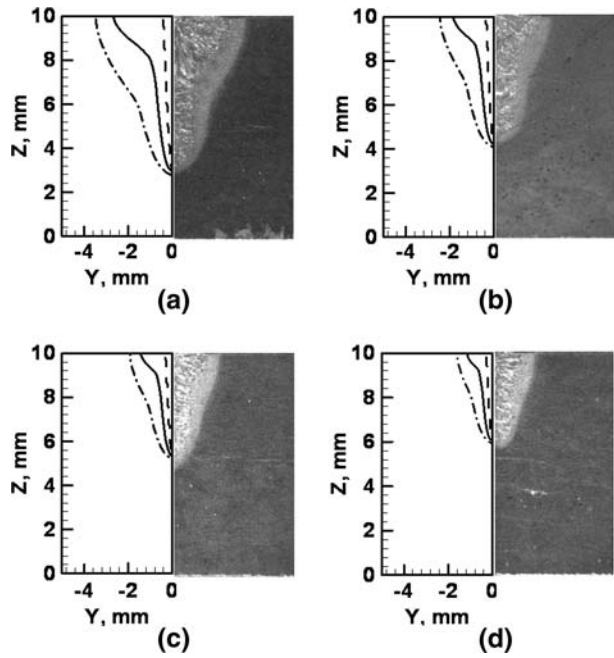
Fig. 2—Comparison of experimental and simulated weld cross sections for the A131 steel for a power of about 5.0 kW and welding speeds of (*a*) 12.7 mm/s, (*b*) 19.1 mm/s, (*c*) 25.4 mm/s, and (*d*) 31.8 mm/s.

point contour marks the cross-sectional geometry of the keyhole, the solidus temperature contour marks the weld pool boundary, and the A1 line contour approximately marks the heat-affected zone region of the welded section. The results show a reasonable agreement between the simulated and calculated weld pool cross sections. The deviation of the simulated weld pool geometry from the experimental results is within the run to run variation of the geometry in the welded samples under seemingly identical experimental conditions.

Figure 1 shows the effect of laser power on weld pool geometry. Figures 1(a) through (c) show partial penetration welds with deep and narrow weld pools having a wide spread near the top due to Maragoni convection. Figure 1(d) shows the weld pool geometry for a full penetration weld. The weld pool widens near the bottom as well as near the top due to Marangoni convection. Figure 2 shows the effect of welding speed on the weld pool geometry. The weld pool geometry is clearly affected by the convection heat transfer as evidenced by the widening of the pool near the top surface where fluid velocities are highest. The geometry shows that for the welding conditions used, convective heat transfer plays an important role. The weld pool dimensions increase with increasing laser power and decreasing welding speed, as expected.

B. Calculated Velocity and Temperature Fields

Figures 3(a) and (b) show the temperature and fluid-flow fields for the symmetry plane and the top plane for a partial penetration and a full penetration weld, respectively. The temperature contours follow the
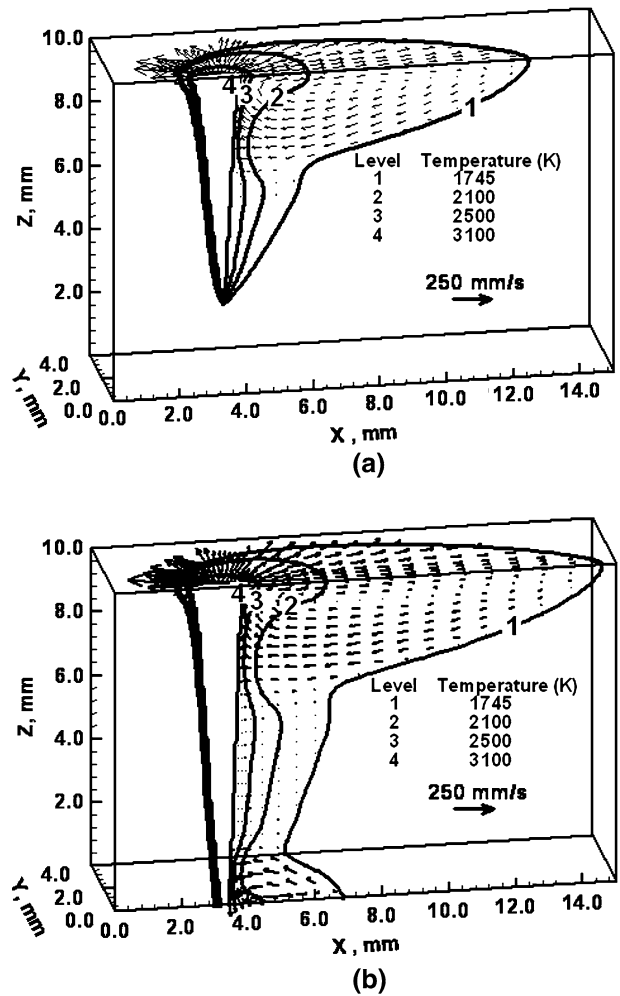

Fig. 3—Top surface and symmetry plane of weld pool with temperature contours and velocity vectors for (*a*) *v* = 12.7 mm/s, 5.0 kW; and (*b*) *v* = 12.7 mm/s, 9.6 kW.

fluid-flow pattern. At the top plane, the liquid metal flows outward from the keyhole and carries heat away from the center. Thus, a wide and elongated weld pool is obtained. The weld pool length decreases with distance from the top surface due to viscous effects and the weld pool is increasingly influenced by conduction heat transfer. Due to the effect of moving heat source, the temperature contours are compressed in the front of the heat source and elongated behind it. For the full penetration weld, the flow pattern at the top surface is similar to that in a partial penetration weld. However, because the weld pool extends to the bottom surface of the workpiece, surface tension–driven Marangoni convective currents are present at the bottom surface that elongate and widen the weld pool. Thus, the weld pool is spread near the top and bottom surfaces and is columnar in between.

Figure 4 shows various temperature contours and velocity vectors for various transverse *y-z* cross sections of the weld pool for partial penetration welding of A131 steel at 5.0-kW laser power and 12.7-mm/s welding speed. The effect of Maragoni convection on the weld
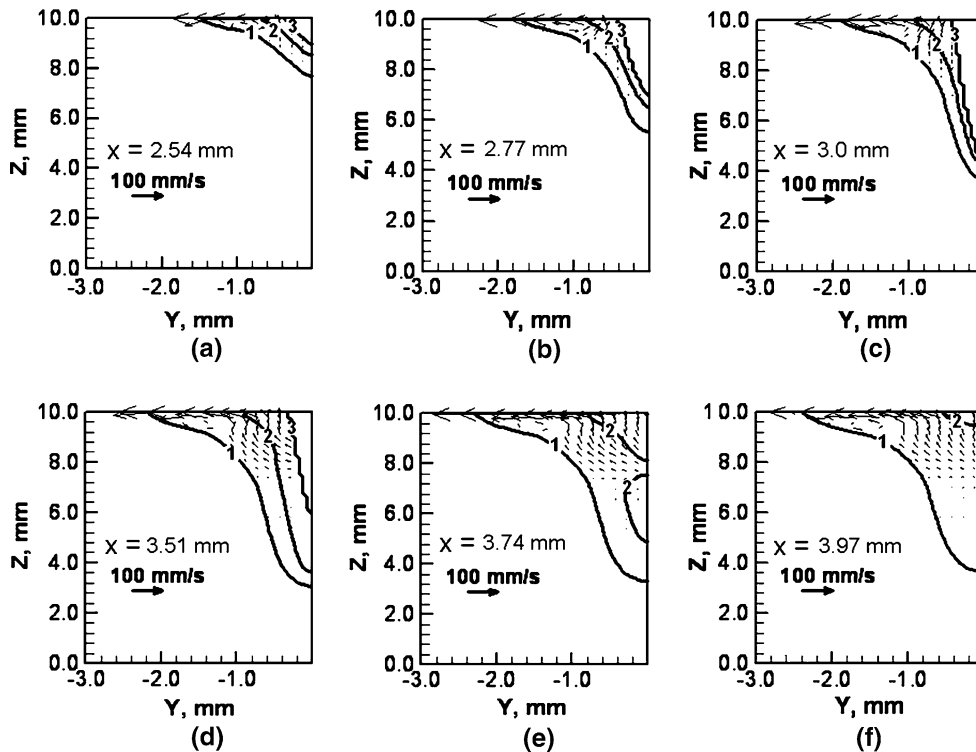
Fig. 4—Weld pool cross-sectional geometry for laser power 5.0 kW and welding speed of 12.7 mm/s, at different locations along the welding directions: (a) x = 2.54 mm, (b) x = 2.77 mm, (c) x = 3.0 mm, (d) x = 3.51 mm, (e) x = 3.74 mm, and (f) x = 3.97 mm. Levels 1, 2, and 3 correspond to 1745, 2500, and 3100, respectively. Laser beam is located at x = 3 mm.

pool size and shape is clearly visible. The circulation currents formed due to Marangoni convection take heat from the center, thus resulting in a wide pool. Highest weld pool depth is obtained for a cross section slightly behind the laser source. For different z levels, maximum weld pool widths are obtained at different x locations.

Figure 5 shows the temperature contours and velocity vectors for various transverse sections of the melted region for full penetration welding of A131 steel at 9.6-kW laser power and 12.7-mm/s welding speed. Marangoni convection currents are seen at the top and bottom surfaces resulting in enhanced heat transfer resulting in a weld pool that is wider at the top and bottom surfaces and narrower in the middle. The weld pool transverse cross section is obtained by the super-imposition of solidus contours on all y-z melted sections.

The relative contribution of convection and conduction depends on the Peclet number (Pe), defined as the ratio of heat transfer by convection to conduction:

$$Pe = \frac{heat_{convection}}{heat_{conduction}} = \frac{u\rho C_p \Delta T}{k \Delta T / L_R} = \frac{u\rho C_p L_R}{k} \quad [21]$$

where u is the typical liquid velocity; ρ is the density; C_p is the specific heat; L_R is the characteristic length, taken as the pool half-width; and k is the thermal conductivity of the liquid. When Pe is much higher than one, heat is transported mainly by convection and the liquid metal circulation in the weld pool markedly affects weld pool geometry. Considering a typical velocity of 100 mm/s, and the properties of the liquid metal, the calculated

Peclet number for A131 steel works out to be of about 50. Thus, convection is the main mechanism of heat transfer.

Figure 6 shows the viscosity contours for different transverse sections along the welding direction for partial penetration welding of A131 steel for an input laser power of 5.0 kW at a welding speed of 12.7 mm/s. Figure 7 is a similar plot for full penetration laser welding of A131 for an input laser power of 9.6 kW at a welding speed of 12.7 mm/s. Highest viscosity values are obtained near the surfaces of the weld pool due to high turbulent contribution arising from very high surface tension driven velocities. Viscosity is lower near the solid-liquid boundary and increases toward the center before decreasing at the liquid-vapor interface in the keyhole.

The fluid flow in the weld pool is turbulent because the flow satisfies Atthey's criteria[37] for turbulence in the weld pool: Reynolds number, $Re = (\rho u_m d/\mu) > 600$, where ρ is density, u_m is maximum velocity, d is pool width, and μ is viscosity. Taking $\rho = 7200$ kg/m³, $u_m = 0.4$ m/s, $d = 0.004$ m, and $\mu = 0.006$ Pa s, the value of Re is 3840. The turbulence in the weld pool is also evident, *post-priori*, from the results in Figure 6. It is observed that the maximum value of the effective viscosity, μ_{eff} ($= \mu_t + \mu$), is about 30 times the laminar viscosity, μ. The symbol μ_t represents turbulent viscosity. The turbulence Reynolds number (TRN), defined as the ratio μ_t/μ, is an indicator of turbulence in the weld pool. Hong *et al.*[38,39] found the weld pool to be turbulent for a local value of TRN of 7.9. Because
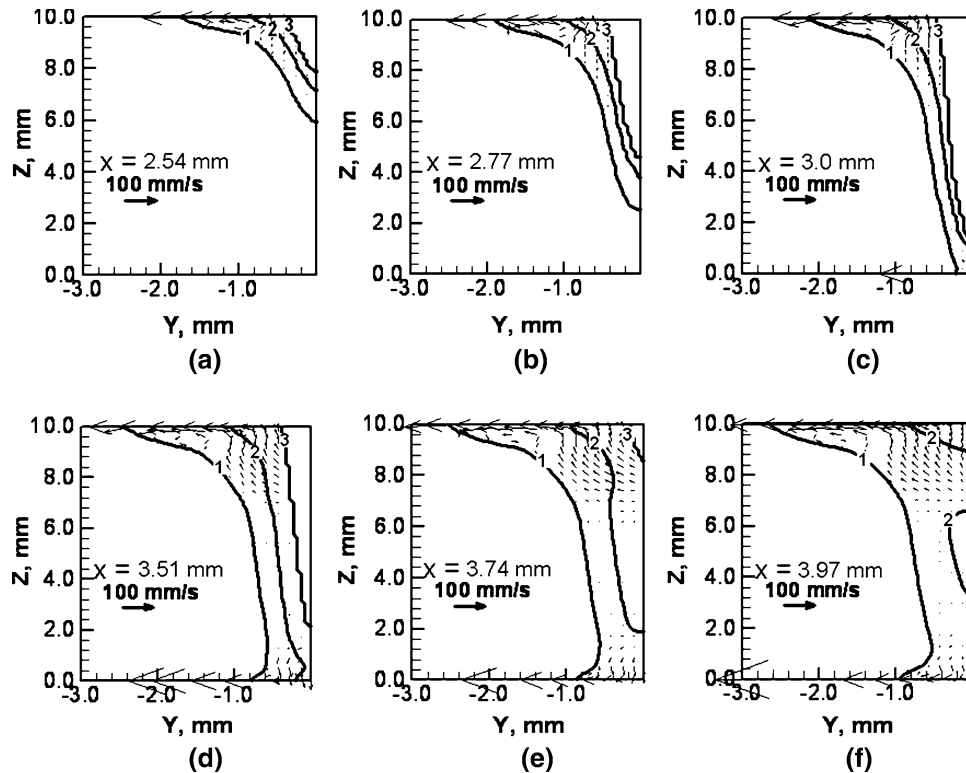
Fig. 5—Weld pool cross-sectional geometry for laser power 5.0 kW and welding speed of 12.7 mm/s, at different locations along the welding direction: (*a*) *x* = 2.54 mm, (*b*) *x* = 2.77 mm, (*c*) *x* = 3.0 mm, (*d*) *x* = 3.51 mm, (*e*) *x* = 3.74 mm, and (*f*) *x* = 3.97 mm. Levels 1, 2, and 3 correspond to 1745, 2500, and 3100 K, respectively. Laser beam is located at *x* = 3 mm.
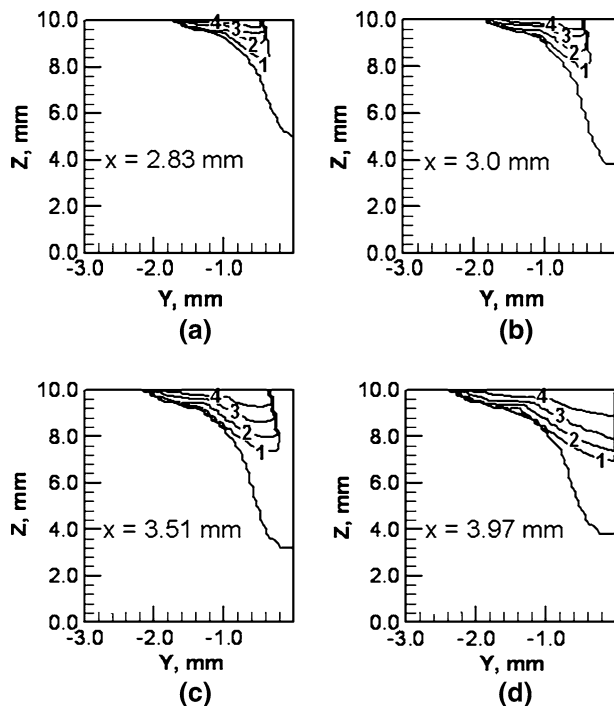

Fig. 6—Viscosity contours for the partial penetration weld done with 5.0-kW laser power at a welding speed of 12.7 mm/s, for the *y-z* cross sections at different locations along the welding direction: (*a*) *x* = 2.83, (*b*) *x* = 3.0 mm, (*c*) *x* = 3.51 mm, and (*d*) *x* = 3.97 mm. Levels 1, 2, 3, and 4 correspond to 0.02, 0.05, 0.1, and 0.2 Pa s, respectively. Laser beam is located at *x* = 3 mm.

Figure 6 shows a maximum value of TRN of about 29, the weld pool is certainly turbulent.

C. *Free Surface*

Figure 8 shows a transverse cross section 1.6 mm behind the laser beam for 9.6-kW laser power and 12.7-mm/s welding speed. The figure shows deformation of the weld pool surfaces under the action of recoil pressure of the metal vapors, surface tension forces, and the pressure due to metal column. The figure shows very little deformation of the top surface for the welding conditions considered. In contrast there is a noticeable hump at the bottom surface where the melt pool area is much smaller and the hump forms because of the recoil pressure and the metallostatic head. Because of the much larger area of the top surface a small depression at the top surface provides enough metal to form the hump at the bottom surface.

The free surface in the keyhole region is governed mainly by the instantaneous vaporization of the metal and the consequent energy balance at the keyhole walls. The free surface calculation here neglects the keyhole region and considers the much larger weld pool surface outside the keyhole. Moreover, because this analysis did not consider the effect of shielding gas flow and solidification the experimentally observed deformation will be different from the calculated values.

For an input laser power of 9.6 kW and absorption coefficient of 0.16, the power absorbed by a single
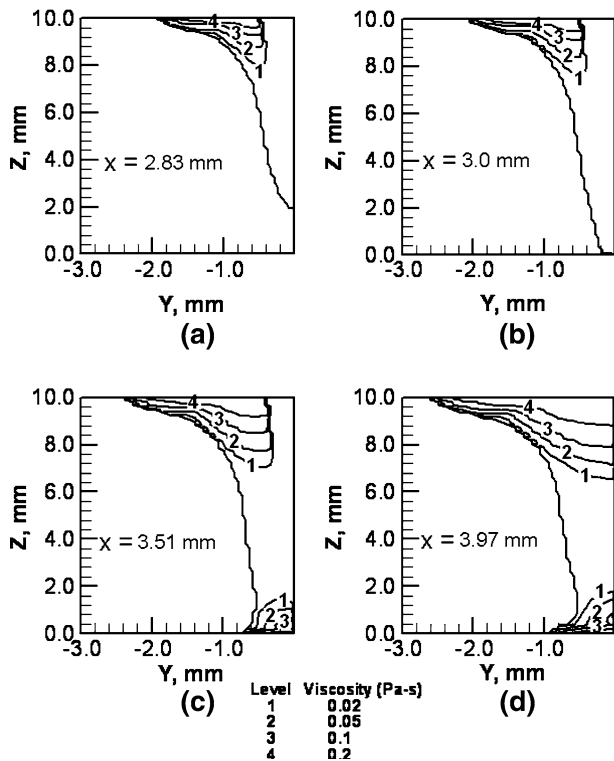
Fig. 7—Viscosity contours for the full penetration weld done with 9.6-kW laser power at a welding speed of 12.7 mm/s, for the *y-z* cross sections at different locations along the welding direction: (*a*) *x* = 2.83, (*b*) *x* = 3.0 mm, (*c*) *x* = 3.51 mm, and (*d*) *x* = 3.97 mm. Levels 1, 2, 3, and 4 correspond to 0.02, 0.05, 0.1, and 0.2 Pa s, respectively. Laser beam is located at *x* = 3 mm.

reflection on the flat surface of the work piece is 1536 W. For the sake of comparison, this power is equivalent to an arc source of 10 V and 220 A with an arc efficiency of about 0.7. The arc pressure at a point (*x,y*) is given as[34,40]

$$P_{arc} = \frac{F}{2\pi\sigma^2} \exp\left(-\frac{x^2 + y^2}{2\sigma^2}\right) \qquad [22]$$

$$F = -0.04791 + 0.0002447 \times I(N) \qquad [23]$$

$$\sigma = 1.4875 + 0.00123 \times I(mm) \qquad [24]$$

where *F* is the total arc force, *I* = 220 A is the arc current, and *σ* is the arc pressure distribution factor. Figure 9 shows a comparison of the recoil pressure calculated for the laser welding with input laser power of 9.6 kW at 12.7-mm/s welding speed with the arc pressure due to an arc current of 220 A. For the conditions described previously, the total recoil force for laser welding process is much smaller than the arc force during the arc welding process. Moreover, considering enhanced absorption of the laser by the workpiece due to multiple reflections, higher arc current will be needed for an equivalent heat input during the arc welding process, resulting in higher arc pressure. This explains the relatively smaller top surface deformation during
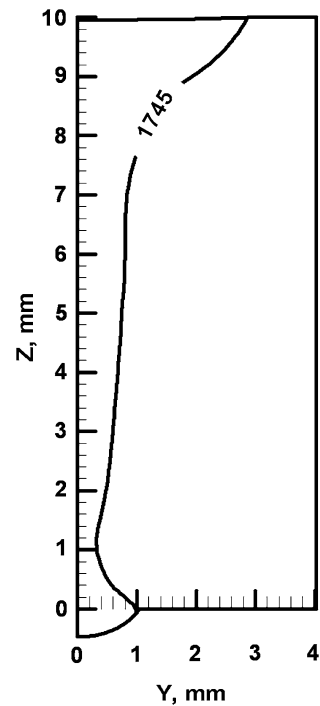

Fig. 8—Deformations of the top and bottom surfaces for 9.6-kW laser power and 12.7-mm/s welding speed at a transverse section 1.6 mm behind the laser beam. The 1745 K contour marks the weld pool boundary.
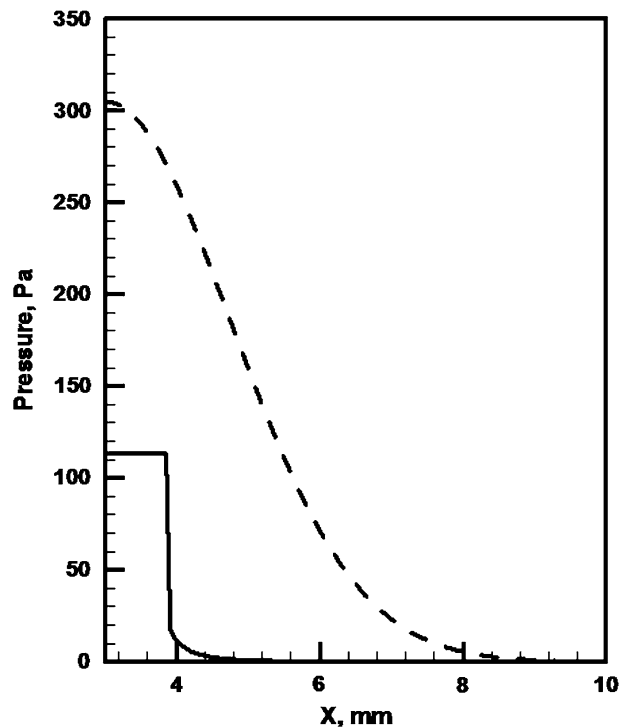

Fig. 9—Calculated pressure variation along the weld centerline. The solid line is for laser welding with input laser power of 9600 W at 12.7-mm/s welding. The dotted line is the arc pressure for a welding current of 220 A. Three millimeters is the starting location of the laser or arc.

laser welding process as compared to an arc welding process with roughly the same heat input.

D. *Solidification*

The solidification microstructure is affected by the solidification rate, R, thermal gradient, G, undercooling, ΔT, and the alloy composition. In this article, possible undercooling has been ignored for simplicity and the solidification characteristics have been calculated considering heat transfer and fluid flow in the weld pool. While G/R determines the solidification morphology, GR determines the scale of the solidification substructure. The values of these parameters have been used to understand the solidification structure. The solidification rate (R) under steady state for linear laser welding is defined in terms of welding velocity (v) as follows:[41]

$$R = v \cos \beta \qquad [25]$$

where β is the angle between the welding direction and the normal at the solid-liquid boundary.

Figure 10(a) shows the calculated temperature gradients for various laser powers. An increase in the laser power increases the weld pool length and the distance over which temperature drops from the boiling point (at keyhole walls) to the solidus temperature. As a result, the average temperature gradient in the weld pool decreases as the laser power in increased. Figure 10(b) shows the variation of the calculated temperature gradient with welding speed. The temperature gradient is affected by two factors. First, with the increase in the welding speed the weld pool is elongated resulting in lower average spatial temperature gradient. Second, when the welding speed is increased, due to decrease in heat input per unit length, the size of the weld pool decreases and temperature gradient increases. For the conditions of the welding shown in Figure 10, and the properties of A131 steel, the latter effect dominates and the temperature gradient increases with increase in welding speed.

The G/R ratio can be used to understand the nature of solidification front. The criterion for plane front instability based on constitutional supercooling is given by the following relation:[1]

$$G/R < \Delta T_E / D_L \qquad [26]$$

where ΔT_E represents the temperature difference between the solidus and liquidus temperatures of the alloy, and D_L is the diffusivity of a solute in the liquid weld metal. For A131 steel, ΔT_E is 40 K and D_L is the solute diffusion coefficient in pure liquid iron, which is of the order of 10^{-7} m^2/s for diffusion of carbon.[42] Thus, $\Delta T/D_L$ is equal to 4×10^2 Ks/mm^2 for solute diffusion in A131 steel. Figures 11(a) and (b) show the variation of G/R with the input power and welding speed, respectively. The magnitude of G/R varies from 1.5 to 3.5 Ks/mm^2, and therefore, the condition of plane front stability is not satisfied at the trailing edge of the weld pool for the range of process parameters considered. The G/R decreases with increase in input power (Figure 11(a)) due to the increase in G, the temperature
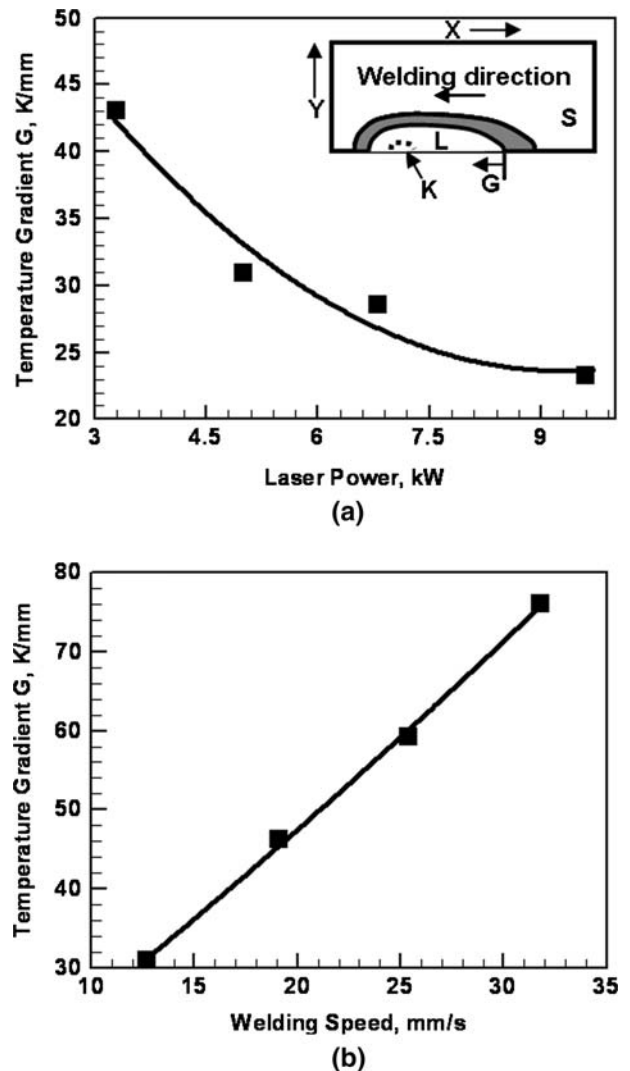

Fig. 10—Calculated values of G at the trailing edge on the weld centerline at the surface for (*a*) different input powers, at 12.7-mm/s welding speed; and (*b*) different welding speeds, at 5.0-kW input power. The symbols indicate the data from numerical simulation, while the solid line indicates the best-fit line. The symbols K, L, and S represent the keyhole, liquid, and solid regions, respectively, and the shaded region between L and S is the two-phase solid-liquid region.

gradient at the trailing edge of the weld pool. The values of G/R do not vary significantly with the increase in welding speed (Figure 11(b)). This is due to the fact that both the temperature gradient G and the solidification rate R increase with increase in welding speed. Thus, the solidification microstructure will become more dendritic with increase in laser power, whereas the change in welding speed will not have a significant effect over the range of experiments considered.

Figure 12 shows the variation of cooling rate, GR, with input laser power and welding speed. The cooling rate at the trailing edge of the weld pool is of the order of 1 K/ms for the range of experiments done. Moreover, the cooling rate decreases with an increase in laser power or decrease in welding speed. With an increase in welding speed, the temperature gradient G as well as the
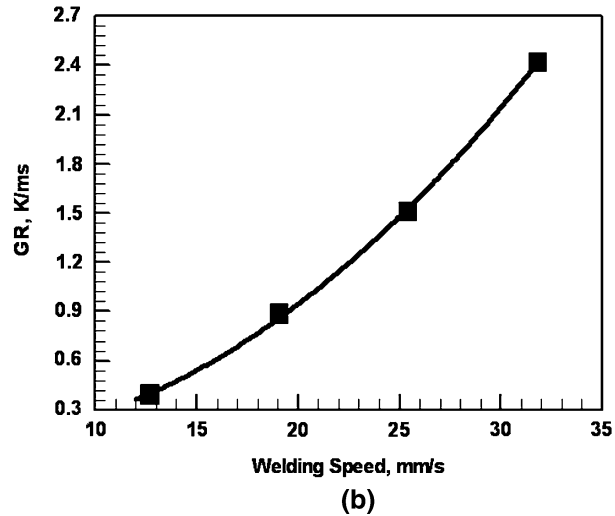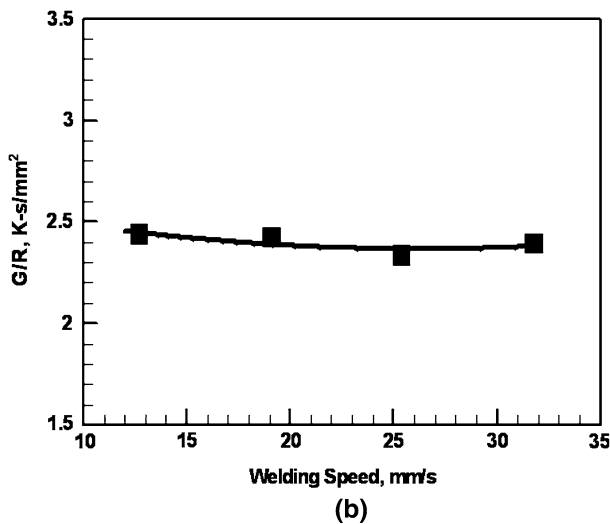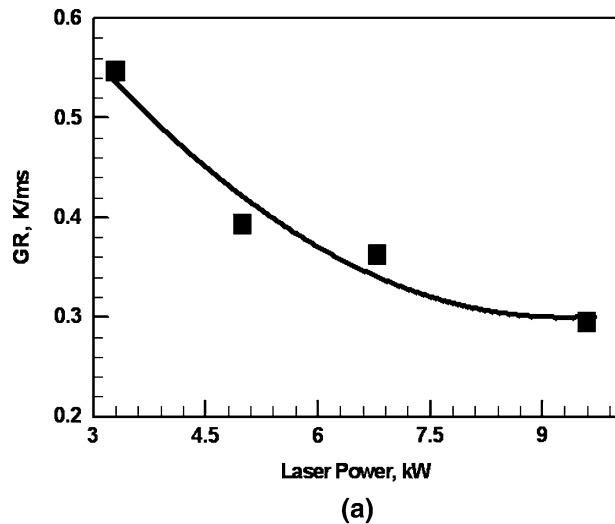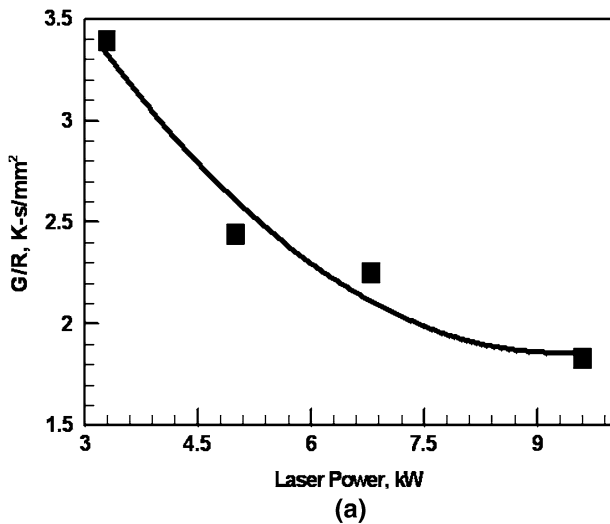
Fig. 11—Calculated values of G/R at the trailing edge on the weld centerline for (*a*) different input powers, at 12.7-mm/s welding speed; and (*b*) different welding speeds, at 5.0-kW input power. The symbols indicate the data from numerical simulation, while the solid line indicates the best-fit line.

Fig. 12—Calculated values of GR at the trailing edge on the weld centerline for (*a*) different input powers, at 12.7-mm/s welding speed; and (*b*) different welding speeds, at 5.0-kW input power. The symbols indicate the data from numerical simulation, while the solid line indicates the best-fit line.

solidification rate R at the trailing edge of the weld pool decreases. However, with increase in laser power, only the temperature gradient at the end of the weld pool decreases whereas the solidification rate remains the same. Thus the cooling rate GR changes more significantly with variation in welding speed than with variation in laser power. If the input laser power increases or the welding speed decreases, the heat input per unit length decreases in the workpiece. Thus, the microstructure will become coarser with increase in heat input per unit length.

Table IV shows the computed solidification parameters for a full penetration weld (9.6 kW, 12.7 mm/s) at the trailing end of the weld pool at different depths. The temperature gradient G is much lower at the top surface ($z = 10$ mm) than at other z values. This is because the length of the weld pool decreases significantly with depth. The local temperature gradient depends also on

Table IV. Solidification Parameters for Different Depths for the Full Penetration Weld (9.6 kW, 12.7 mm/s); G is Calculated along the Welding Direction and at the Rear End of the Weld Pool

Z (mm)	G (K/mm)	GR (K/ms)	G/R (K s/mm^2)
0	150	1.9	11.8
1.5	144	1.8	11.3
5	223	2.8	17.6
10	23	0.3	1.8

the fluid pattern and therefore a shorter weld pool does not always correspond to a higher temperature gradient. For example, the weld pool is shortest at $z = 1.5$ mm, but the temperature gradient at the trailing edge for this z is not the largest. For $z = 5$ mm, the fluid velocities are very small and the small convective heat-transfer
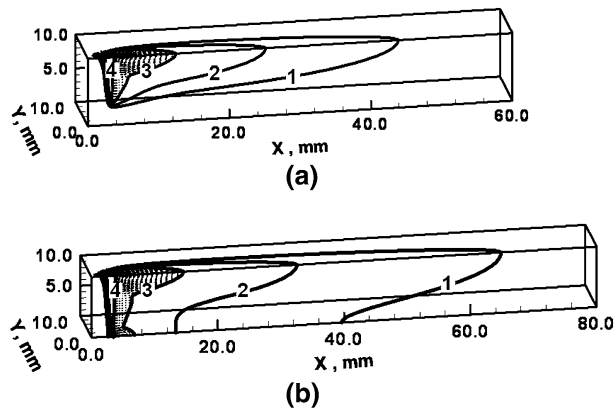
Fig. 13—Temperature contours for (*a*) 5000 W, 12.7 mm/s; and (*b*) 9600 W, 12.7 mm/s. Levels 1, 2, 3, and 4 correspond to 773, 1073, 1745, and 3100 K, respectively.

results in higher *G* values. In general, however, *G* and, correspondingly, *G/R* and *GR* will be higher than the respective values at the top surface. Thus, the microstructure in the interior of the weld zone will be finer and less dendritic than at the top surface.

For partial penetration welds, the temperature contours converge toward the bottom of the keyhole. That is, the separation between any two temperature contours becomes small near the bottom of the weld as shown in Figure 13(a). Thus, the cooling time from 1073 to 773 K becomes small and the cooling rate becomes high near the bottom of the weld pool. On the other hand, the temperature contours are spread out near the bottom for a full penetration weld. Therefore, the cooling time from 1073 to 773 K does not decrease significantly near the bottom and a much lower cooling rate is obtained. Figure 14 shows the average cooling rates from 1073 to 773 K for a partial penetration and a full penetration weld at the symmetry plane. The cooling rate is very high at the lower part of the partial penetration weld compared to the full penetration weld.

The cooling rates give an indication of the scale of microstructure of the welds. A higher cooling rate at the trailing edge of the weld pool, *GR*, indicates faster cooling at all locations of the weldment. Relatively higher cooling rates result in finer microstructures, as can be observed by comparing Figure 15(a) with Figure 15(b) and Figure 16(a). Figure 15 shows the microstructures for the highest and the lowest heat input per unit length used to make the welds. The heat input per unit length for Figure 15(a), 756 J/mm (9.6-kW laser power at 12.7-mm/s welding speed), is several times higher than that for Figure 15(b), 157 J/mm (5.0-kW laser power and 31.8 mm/s). Consequently, the cooling rate for the higher heat input weld was much slower than that for the lower heat input weld, and this difference is apparent in the scale of the microstructures of the two cases. The higher cooling rate for the lower heat input per unit length weld is responsible for the finer microstructure in Figure 15(b) as compared to Figure 15(a) near the weld centerline. The figures also show prior austenitic grain boundaries.
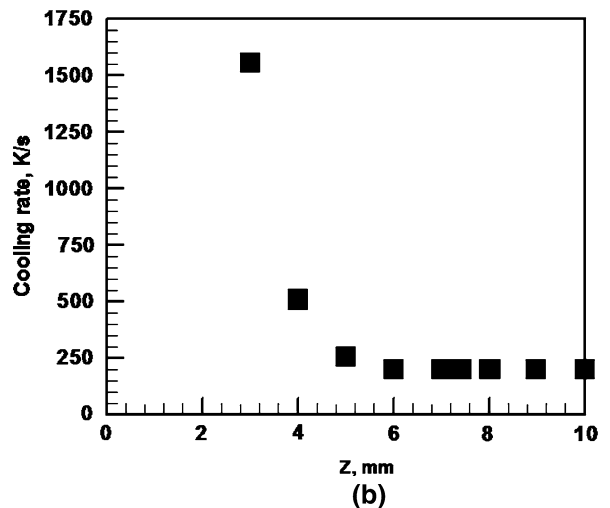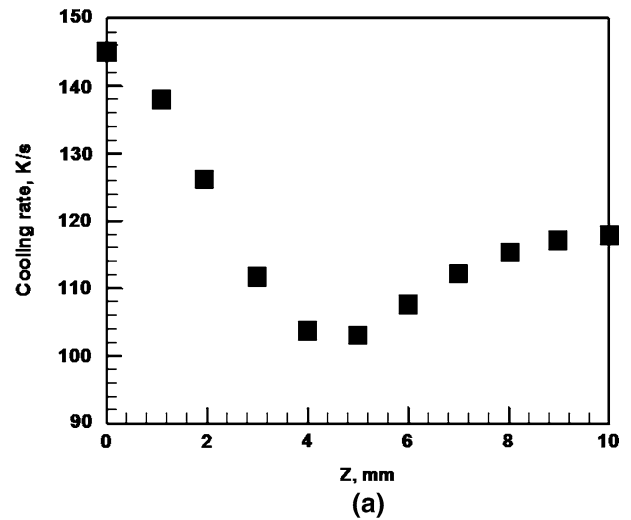

Fig. 14—The 1073 to 773 K cooling rate at the symmetry plane for (*a*) 9600 W, 12.7 mm/s; and (*b*) 5000 W, 12.7 mm/s.

Figures 16(a) and (b) show the microstructures near the bottom of a partial penetration weld (5 kW, 12.7 mm/s) and a full penetration weld (9.6 kW, 12.7 mm/s), respectively. The microstructure for the full penetration weld in Figure 16(b) is much coarser than that for the partial penetration weld shown in Figure 16(a). This is due to the higher heat input per unit length and consequently much slower cooling in the full penetration case.

V. SUMMARY AND CONCLUSIONS

A computationally efficient model of heat and fluid flow in keyhole mode laser welding was tested over a range of welding velocities and laser powers for partial and full penetration welds. For the calculation of turbulent viscosity, a model based on Prandtl's mixing length hypothesis was used under the assumption that the turbulent kinetic energy is a certain fraction of mean kinetic energy. The model was used to predict weld
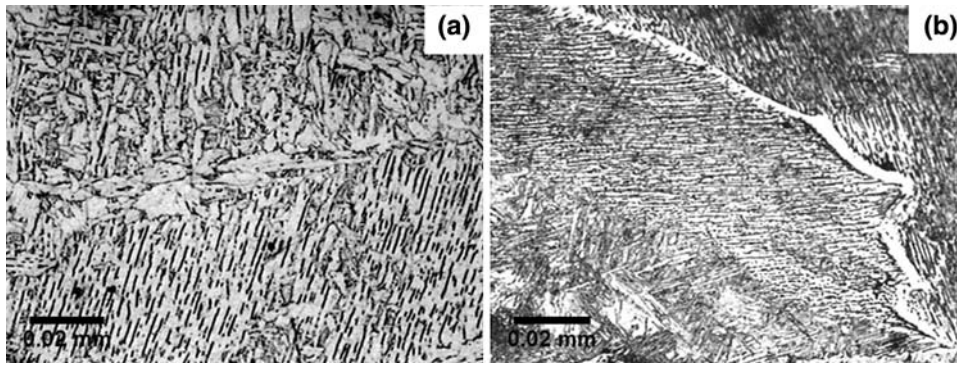
Fig. 15—Microstructural scale for (a) 9.6 kW, 12.7 mm/s; and (b) 5.0 kW, 31.8 mm/s.
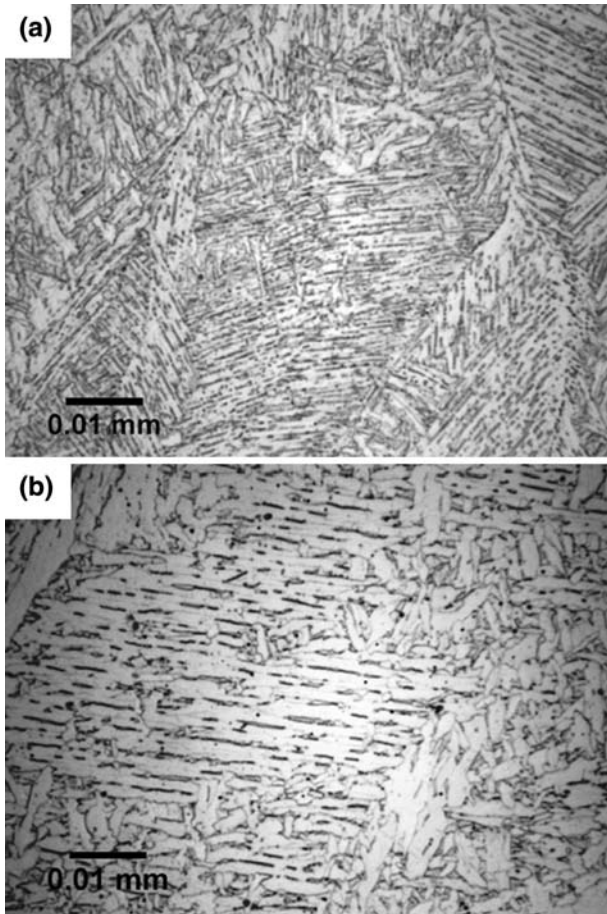

Fig. 16—Microstructure along the weld centerline (a) near the bottom of a partial-penetration weld (5.0 kW, 12.7 mm/s) and (b) near the bottom of a full-penetration weld (9.6 kW, 12.7 mm/s).

geometry, temperature, and velocity fields for partial and full penetration welds covering a wide range of welding variables. The calculation scheme was computationally efficient and the time taken for convergence was less than 30 minutes for all cases.

For the conditions of welding, convection is the main mechanism of heat transfer in the laser welding of stainless steels. Keyhole formation results in a deep weld pool that has a spread at the top surface due to surface tension driven convective currents. For full penetration weld, the weld pool becomes wide and elongated both at the top as well as the bottom surfaces due to Marangoni convection. The calculated weld geometries agreed reasonably well with the experimental results for the range of welding speed and laser power tested. Turbulence was found to be more important in regions near the top surface for partial penetration welds and for both top and bottom surfaces for the full penetration welds, as indicated by the high turbulent viscosity values. Free surface calculations showed a hump at the bottom surface of the full penetration weld. The calculated top surface deformation was very small.

Calculation of solidification parameters showed that the criterion of plane front stability is not satisfied at the trailing edge of the weld pool. The solidification microstructure tends to become more dendritic with increase in laser power, and coarser with increase in heat input per unit length. The microstructure also varies with location due to spatial variation of the cooling rate.

APPENDIX I

Because the orientation of keyhole is almost vertical, the heat transfer at the keyhole wall takes place mainly along the horizontal plane. A heat balance on the keyhole wall gives the following relation for local keyhole wall angle θ:[7,8]

$$\tan(\theta) = \frac{I_c}{I_a - I_v} \qquad [\text{Ia}]$$

where I_c is the radial heat flux conducted into the keyhole wall, I_a is the locally absorbed beam energy, and I_v is the evaporative heat flux on the keyhole wall. The value of I_c is obtained from a 2-D temperature field in an infinite plate with reference to a linear heat source. The term I_c is defined as

$$I_c(r, \varphi) = -\lambda \frac{\partial T(r, \varphi)}{\partial r} \qquad [\text{Ib}]$$

where (r, φ) designates the location in the plate with the line source as the origin, T is the temperature, and λ is

the thermal conductivity. The 2-D temperature field can be calculated considering the conduction of heat from the keyhole wall into the infinite plate as[41]

$$T(r, \varphi) = T_a + \frac{P'}{2\pi\lambda} K_0(\Omega r) e^{-\Omega r \cos \varphi} \qquad \text{[Ic]}$$

where T_a is the ambient temperature, P' is the power per unit depth, $K_0()$ is the solution of the second kind and zero-order modified Bessel function, and $\Omega = v/(2\kappa)$, where v is the welding speed and κ is the thermal diffusivity.

The locally absorbed beam energy flux, I_a, on the keyhole wall that accounts for the absorption during multiple reflections and the plasma absorption is calculated as[8]

$$I_a = e^{-\beta l}\left(1 - (1 - \alpha)^{1+\pi/4\theta}\right)I_0 \qquad \text{[Id]}$$

where β is the inverse Bremsstrahlung absorption coefficient of plasma, l is the average path of the laser beam in plasma before it reaches the keyhole wall, α is the absorption coefficient of the work piece, θ is the average angle between the keyhole wall and the initial incident beam axis, and I_0 is the local incident beam intensity that varies with depth from the surface and radial distance from the beam axis.[8] Constant laser beam absorption coefficient, independent of location, is assumed for the plasma in the keyhole and for the laser beam absorption at the keyhole wall. The keyhole profile is first calculated without considering multiple reflections. With the approximate keyhole dimensions, the average angle between the keyhole wall and incident beam axis is then calculated.[8]

The factor $1 + \frac{\pi}{4\theta}$ represents the average number of reflections that a laser beam undergoes before leaving the keyhole.[8] When a laser beam of intensity I_0 traverses a length l in the plasma before reaching the material surface, $(1 - e^{-\beta l})I_0$ is absorbed by the plasma. Of the remaining $-e^{-\beta l}I_0$ that falls on the material, $(1 - \alpha) - e^{-\beta l}I_0$ is reflected. After $1 + \frac{\pi}{4\theta}$ reflections, $(1 - \alpha)^{1+\pi/4\theta}e^{-\beta l}I_0$ of the intensity is reflected and the remaining $(1 - (1 - \alpha)^{1+\pi/4\theta})e^{-\beta l}I_0$ is absorbed. For $\alpha = 0.16$ and $1 + \frac{\pi}{4\theta} = 6$, $l = 0.5$ mm, about 5 pct of the local beam intensity is absorbed by the plasma,[44,45] about 65 pct is absorbed by the material, and the remaining 30 pct leaves the keyhole.

The evaporative heat flux, I_v, on the keyhole wall is given as

$$I_v = \sum_{i=1}^{n} J_i \Delta H_i \qquad \text{[Ie]}$$

where n is the total number of alloying elements in the alloy, ΔH_i is the heat of evaporation of element i, and J_i is the evaporation flux of element i given by the modified Langmuir equation:[46–48]

$$J_i = \frac{a_i P_i^0}{7.5} \sqrt{\frac{M_i}{2\pi R T_b}} \qquad \text{[If]}$$

where a_i is the activity of element i, P_i^0 is the equilibrium vapor pressure of element i over pure liquid at the boiling point T_b, and M_i is the molecular weight of element i. The factor 7.5 is used to account for the diminished evaporation rate at one atmosphere pressure compared to the vaporization rate in vacuum and is based on previous experimental results.[46,47]

APPENDIX II

Recoil pressure exerted by the metal vapors can be given by the difference between the momentum of the vapors leaving the surface and the z-direction momentum of the liquid near the liquid-vapor interface.

$$P_{\text{rec}} = \rho_g v_g^2 - \rho_l v_l^2 \qquad \text{[IIa]}$$

The subscripts g and l stand for gas and liquid, respectively, and the velocities normal to the liquid-vapor interface. Because, by mass conservation,

$$\rho_g v_g = \rho_l v_l \text{ and } \rho_g \ll \rho_l \qquad \text{[IIb]}$$

$$v_g \gg v_l \qquad \text{[IIc]}$$

Therefore,

$$P_{\text{rec}} = (\rho_g v_g) v_g - (\rho_l v_l) v_l = (\rho_g v_g)(v_g - v_l) \approx \rho_g v_g^2 \qquad \text{[IId]}$$

$$P_{\text{rec}} \approx J_g v_g \qquad \text{[IIe]}$$

where J_g is the vaporization flux, which can be calculated from the Langmuir equation given in Eq. [IIf]:

$$v_g = J_g/c \qquad \text{[IIf]}$$

where c is the concentration of the metal vapors and is given by

$$c = \frac{M p_v}{R T} \qquad \text{[IIg]}$$

where M is the molecular weight of iron, and p_v is the vapor pressure of iron at temperature T, calculated from an empirical relation.[49]

REFERENCES

1. T. DebRoy and S.A. David: *Rev. Mod. Phys.*, 1995, vol. 67, pp. 85–112.
2. D.E. Swift-Hook and A.E.F. Gick: *Weld. J. (Miami)*, 1973, vol. 52, pp. 492s–499s.
3. J.G. Andrews and D.R. Atthey: *J. Phys. D: Appl. Phys.*, 1976, vol. 9, pp. 2181–94.
4. J. Kroos, U. Gratzke, and G. Simon: *J. Phys. D: Appl. Phys.*, 1993, vol. 26, pp. 474–80.
5. J. Mazumder and W.M. Steen: *J. Appl. Phys.*, 1980, vol. 51, pp. 941–47.
6. E.A. Metzbower: *Metall. Trans. B*, 1993, vol. 24A, pp. 875–80.
7. A. Kaplan: *J. Phys. D: Appl. Phys.*, 1994, vol. 27, pp. 1805–14.
8. H. Zhao and T. DebRoy: *J. Appl. Phys.*, 2003, vol. 93, pp. 10089–10096.
9. R. Rai and T. DebRoy: *J. Phys. D: Appl. Phys.*, 2006, vol. 39, pp. 1257–66.

10. R. Rai, G.G. Roy, and T. DebRoy: *J. Appl. Phys.*, 2007, vol. 101 (5), Art. No. 054909.
11. H. Ki, P.S. Mohanty, and J. Mazumder: *Metall. Mater. Trans. A*, 2002, vol. 33A, pp. 1817–30.
12. H. Ki, P.S. Mohanty, and J. Mazumder: *Metall. Mater. Trans. A*, 2002, vol. 33A, pp. 1831–42.
13. J. Dowden, M. Davis, and P. Kapadia: *J. Fluid Mech.*, 1983, vol. 126, pp. 123–46.
14. J. Dowden, N. Postacioglu, M. Davis, and P. Kapadia: *J. Phys. D: Appl. Phys.*, 1987, vol. 20, pp. 36–44.
15. N. Postacioglu, P. Kapadia, M. Davis, and J. Dowden: *J. Phys. D: Appl. Phys.*, 1987, vol. 20, pp. 340–45.
16. P.G. Klemens: *J. Appl. Phys.*, 1976, vol. 47, pp. 2165–74.
17. W. Sudnik, D. Radaj, and W. Erofeew: *J. Phys. D: Appl. Phys.*, 1996, vol. 29, pp. 2811–17.
18. R.B. Bird, W.E. Stewart, and E.N. Lightfoot: *Transport Phenomena*, Wiley, New York, NY, 1960.
19. S.V. Patankar: *Numerical Heat Transfer and Fluid Flow*, Hemisphere Publishing Corporation, New York, NY, 1980.
20. V.R. Voller and C. Prakash: *Int. J. Heat Mass Transfer*, 1987, vol. 30, pp. 1709–19.
21. A.D. Brent, V.R. Voller, and K.J. Reid: *Numer. Heat Transfer Part A*, 1988, vol. 13, pp. 297–318.
22. K. Mundra, T. DebRoy, and K.M. Kelkar: *Numer. Heat Transfer Part A*, 1996, vol. 29, pp. 115–29.
23. A. Kumar and T. DebRoy: *J. Appl. Phys.*, 2003, vol. 94, pp. 1267–77.
24. S. Kou and D.K. Sun: *Metall. Trans. A*, 1985, vol. 16A, pp. 203–13.
25. C.H. Kim, W. Zhang, and T. DebRoy: *J. Appl. Phys.*, 2003, vol. 94, pp. 2667–79.
26. A. De and T. DebRoy: *J. Phys. D: Appl. Phys.*, 2004, vol. 37, pp. 140–50.
27. A. De and T. DebRoy: *J. Appl. Phys.*, 2004, vol. 95 (9), pp. 5230–39.
28. W. Pitscheneder, T. DebRoy, K. Mundra, and R. Ebner: *Weld. J. (Miami)*, 1996, vol. 75, pp. 71s–80s.
29. H. Zhao and T. DebRoy: *Metall. Mater. Trans. B*, 2001, vol. 32B, pp. 163–72.
30. D.C. Wilcox: *Turbulence Modeling for CFD*, DCW Industries, La Canada, CA, 1993.
31. B.E. Launder and D.B. Spalding: *Lectures in Mathematical Models of Turbulence*, Academic Press, London, 1972.
32. K. Hong: Ph.D. Thesis, University of Waterloo, Waterloo, 1996, pp. 145–46.
33. Z. Yang and T. DebRoy: *Metall. Mater. Trans. B*, 1999, vol. 30B, pp. 483–93.
34. W. Zhang, C.L. Kim, and T. DebRoy: *J. Appl. Phys.*, 2004, vol. 95, pp. 5210–19.
35. W. Zhang, C.L. Kim, and T. DebRoy: *J. Appl. Phys.*, 2004, vol. 95, pp. 5220–29.
36. R.L. Ketter and S.P. Prawel: *Modern Methods of Engineering Computation*, McGraw-Hill, New York, NY, 1969.
37. D.R. Atthey: *J. Fluid Mech.*, 1980, vol. 98, pp. 787–801.
38. K. Hong, D.C. Weckman, A.B. Strong, and W. Zheng: *Sci. Technol. Weld. Joining*, 2002, vol. 7, pp. 125–36.
39. K. Hong, D.C. Weckman, A.B. Strong, and W. Zheng: *Sci. Technol. Weld. Joining*, 2003, vol. 8, pp. 313–24.
40. M.L. Lin and T.W. Eagar: *Metall. Trans. B*, 1986, vol. 17B, pp. 601–07.
41. X. He, J. Elmer, and T. DebRoy: *J. Appl. Phys.*, 2005, vol. 97, Art. No. 84909.
42. H. Geiger and D.R. Poirier: *Transport Phenomena in Metallurgy*, Addison Wesley, London, 1973.
43. D. Rosenthal: *Trans. ASME*, 1946, vol. 48, pp. 849–66.
44. R. Miller and T. DebRoy: *J. Appl. Phys.*, 1990, vol. 68 (5), pp. 2045–50.
45. M.M. Collur and T. DebRoy: *Metall. Trans. B*, 1989, vol. 20B, pp. 277–86.
46. A. Block-Bolten and T.W. Eagar: *Metall. Trans. B*, 1984, vol. 15B, pp. 461–69.
47. M.M. Collur, A. Paul, and T. DebRoy: *Metall. Trans. B*, 1987, vol. 18B, pp. 733–40.
48. P. Sahoo, M.M. Collur, and T. DebRoy: *Metall. Trans. B*, 1988, vol. 19B, pp. 967–72.
49. E.A. Brandes and G.B. Brook, eds., *Smithells Metals Reference Book*, 7th ed., Butterworth Heinemann, Woburn, MA, 1992, pp. 8–51.